

X-ray mass attenuation coefficients and imaginary components of the atomic form factor of zinc over the energy range of 7.2–15.2 keV

Nicholas A. Rae, Christopher T. Chantler, and Zwi Barnea
School of Physics, University of Melbourne, Victoria 3010, Australia

Martin D. de Jonge
Australian Synchrotron, Victoria 3168, Australia

Chanh Q. Tran
La Trobe University, Victoria 3086, Australia

James R. Hester
Australian Nuclear Science and Technology Organisation, New South Wales 2234, Australia
 (Received 16 July 2009; published 22 February 2010)

The x-ray mass attenuation coefficients of zinc are measured in a high-accuracy experiment between 7.2 and 15.2 keV with an absolute accuracy of 0.044% and 0.197%. This is the most accurate determination of any attenuation coefficient on a bending-magnet beamline and reduces the absolute uncertainty by a factor of 3 compared to earlier work by advances in integrated column density determination and the full-foil mapping technique described herein. We define a relative accuracy of 0.006%, which is not the same as either the precision or the absolute accuracy. Relative accuracy is the appropriate parameter for standard implementation of analysis of near-edge spectra. Values of the imaginary components f'' of the x-ray form factor of zinc are derived. Observed differences between the measured mass attenuation coefficients and various theoretical calculations reach a maximum of about 5% at the absorption edge and up to 2% further than 1 keV away from the edge. The measurements invite improvements in the theoretical calculations of mass attenuation coefficients of zinc.

DOI: [10.1103/PhysRevA.81.022904](https://doi.org/10.1103/PhysRevA.81.022904)

PACS number(s): 32.80.Aa, 32.80.Fb, 32.30.Rj, 61.05.cj

I. INTRODUCTION

The x-ray atomic form factor is the fundamental parameter describing the interaction of x rays with matter. Accurate values of the mass attenuation coefficient and hence of the dielectric function are vital for many areas such as particle energy loss functions [1], electron energy loss spectroscopy [2], crystallography [3,4], tomography [5], and polarizability and reflectometry [6]. A wide range of atomic [7], molecular [8], and solid-state [9,10] features can be calculated given accurate values of x-ray atomic form factors of the constituent elements.

Theoretical estimates of atomic form factors have been tabulated since early in the development of x-ray science for all elements across a wide range of energies. The National Institute of Standards and Technology (NIST) currently supports two such tabulations; XCOM [11,12] and FFAST [13–15]. Significant differences exist in the values of the form factors from these tabulations across a wide range of energies and elements [13,16], the largest being at and immediately above absorption edges [17]. These discrepancies lead to a significant problem when calculating mass attenuation coefficients in these regions.

Figure 1 shows the percentage difference between various experimentally or theoretically determined mass attenuation coefficients of zinc and the corresponding theoretical values calculated using FFAST. Despite experimental errors between 1% and 2% quoted by the various authors, the values are inconsistent, have a spread of about 10%, and generally do not agree with theoretical values. Above the absorption edge

at 9.623 keV, there are few reported measurements of mass attenuation coefficients of zinc. Given these inconsistencies, uncertainty, and spread, existing experimental results cannot be used to distinguish different theoretical approaches (Fig. 1).

The absorption edge region is of particular importance for widely used synchrotron techniques such as x-ray absorption fine structure (XAFS) [22] and x-ray absorption near-edge structure (XANES) [9]. The need for accurate measurements of the mass attenuation coefficient in this region has been noted by other groups [23] and in particular the measurement of K-shell [24] and L-shell [25] jump factors and jump ratios has been of concern. Investigation of photoeffect cross sections for subshells depends upon accurate experimental data and should preferably cover a range of energies to avoid key systematics [26]. In the edge region, accurate values of the mass attenuation coefficient are needed to derive structural and chemical information, such as for example elemental and phase concentrations derived from the edge height [27].

The discrepancies between theory and experiment, between theory and theory, and between experiment and experiment led the International Union of Crystallography (IUCr) to conduct a study of problems associated with the measurement of x-ray mass attenuation coefficients [28,29]. The study found that systematic errors had not been quantified, leading to discrepancies greater than the individual measured uncertainty. Such measurements could not be used to distinguish among different theoretical approaches. The study found that a key tool for determining sources of error was to perform measurements on different thicknesses of absorbing material.

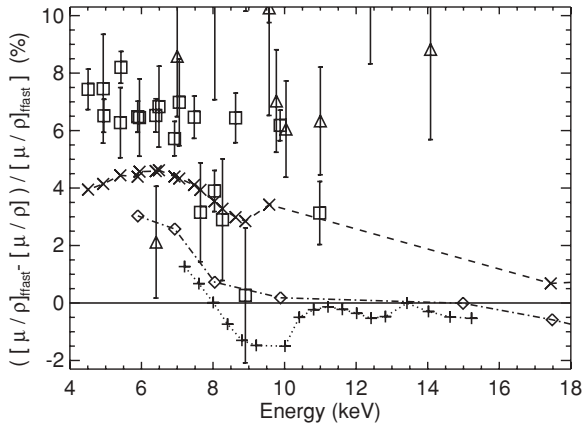


FIG. 1. Experimental and theoretical values of the mass attenuation coefficients of zinc displayed as a percentage difference from the FFAST tabulated values [14,15]. Experimental results (Δ , Hopkins [18]; \square , Unonius and Suortti [19]) are plotted with quoted error bars. Few results have been published in the region above the K-edge (9.623 keV). For such an important element, this dearth of information is surprising and limits detailed bonding and chemical analysis. There are significant discrepancies between experimental results, often larger than the reported error. Tabulated theoretical values include XCOM [11,12] (dotted line with + marking tabulated energies) and Creagh and McAuley [20] (dashed line with \times marking energies tabulated in the International Tables for Crystallography). The dot-dash line shows the experimental-theoretical values of Henke *et al.* [21] with the \diamond symbol marking the tabulated energies.

This varies the attenuation at a given energy, allowing the functional form of some systematic errors to be identified.

Recent measurements of mass attenuation coefficients of molybdenum, silver, copper, and tin by our group have revealed significant systematic differences between measurements and theory in the region of the K-edge [30–34], including the region important for studies of XAFS [35], XANES [36,37] and differential XAFS [38]. The current study investigates the x-ray attenuation coefficients of zinc, an element with wide applications in industrial, catalytic, and biomedical fields, in an energy region including the K absorption edge. Discrepancies between theory and experiment have been noted by other authors [39] for different metal foils [40,41] and vapors [42]. The current study is the first high-accuracy experiment on zinc. A new method for the absolute mapping of the integrated column density and changes to the experimental data collection have reduced the experimental error bars by a factor of 3 compared to earlier work. This is the most accurate measurement carried out on a bending-magnet beamline. Hence this study makes it possible to investigate anomalies for zinc.

In the present study, we have employed the x-ray extended range technique (XERT), which makes use of multiple foils and a wide range of energies to measure mass attenuation coefficients on an absolute scale [43–48]. The XERT approach allows testing for a range of systematic errors, corrections for which are applied. A new method to determine the integrated column density [49] [the density of the absorber along the path of the x-ray beam as described in Eq. (5) later] is described which further improves the accuracy of the measured mass attenuation coefficients.

This paper investigates sources of systematic error and presents corrected, beamline-independent measurements of the x-ray mass attenuation of zinc between 7.2 and 15.2 keV with accuracies of between 0.044% and 0.197%. A comparison is then made between our measurements and theoretical tabulations, and discrepancies of up to 5% are found. The mass attenuation coefficient, the photoelectric mass absorption coefficient, and the imaginary component of the form factor are determined after subtraction of Rayleigh and Compton scattering cross sections (Table I).

In Table I, we introduce the *relative accuracy*, as opposed to precision or absolute accuracy, of the mass attenuation coefficient. The relative accuracy is the uncertainty in the mass attenuation coefficient relevant for XAFS and XANES analysis. Specifically, it is the uncertainty estimate based on statistics and all possible systematics which affect the near-edge structure but not including the absolute scaling of the amplitude of that structure. In other words, the relative accuracy omits the uncertainty in determining the absolute value of the mass attenuation coefficient (cm^2/g) but requires that all measurements be accurately located on the same relative scale.

An accuracy in, for example, SI units for relevant axes must always be *absolute*, and precision is always the local reproducibility. However, we have proven in past work that many systematic errors in typical measurements are much greater than the estimate of reproducibility in a particular experiment, especially when (as is common) parameter space is not carefully investigated. Many experiments do not (even) provide a robust estimate of reproducibility, but it is always important for critical analysis to provide as robust a measurement of accuracy as possible. Some systematics contribute directly to an investigation of relative structure such as is investigated in XAFS analysis, where the scale and height of features may be referenced to an arbitrary edge height. Investigating systematics which contribute to this latter study is important and is presented in this paper. Careful and correct propagation of experimental uncertainties is needed for the evaluation and improvement of XAFS models [50].

II. EXPERIMENTAL DETAILS

The x-ray beam was produced using the bending-magnet beamline 20BM at the Australian National Beamline Facility of the Photon Factory synchrotron in Tsukuba, Japan. Figure 2 shows the layout of the experimental components. A Si(111) double-reflection monochromator was used to select the beam with a small energy bandwidth of order 3 eV [51]. Slits defined the beam size to be 0.5 mm high by 2 mm wide. The Big Diff, a large powder diffraction chamber [52], was used to determine the beam energy and energy bandwidth using powder diffraction patterns of NIST Standard Reference Material (SRM) Si 640c [53].

Downstream from the powder diffractometer was the experimental table with the specimen stage. Ion chambers and daisy wheels were placed symmetrically upstream and downstream of the zinc foil absorbing specimens to monitor the incident and attenuated x-ray beam. Between the ion chambers and the zinc foils, apertures and secondary foils were mounted on daisy wheels to measure the angular dependence

TABLE I. Mass attenuation coefficients $[\frac{\mu}{\rho}]$ and the imaginary component of the form factor, f'' , as a function of energy. The total one-standard-deviation uncertainty is presented in brackets after the number. The relative absolute accuracy of the mass attenuation coefficient is presented as the $\sigma([\frac{\mu}{\rho}])_r$, percentage relative accuracy error in column 3, and as the percentage (absolute) accuracy $\sigma([\frac{\mu}{\rho}])_a$ in column 4. Column 5 lists the photoelectric mass absorption coefficient $[\frac{\mu}{\rho}]_{pe}$, derived by subtracting the mass attenuation due to Rayleigh and Compton scattering, $[\frac{\mu}{\rho}]_{R+C}$ (column 6) from the total mass attenuation coefficient in column 1, in order to derive the form factor f'' in column 7 using Eq. (12). The uncertainty in $[\frac{\mu}{\rho}]_{R+C}$ is estimated by half the discrepancy between tabulations in XCOM and FFAST and is included in the uncertainty of f'' .

Energy (keV)	$[\frac{\mu}{\rho}]$ (cm ² /g)	$\sigma([\frac{\mu}{\rho}])_r$ % relative	$\sigma([\frac{\mu}{\rho}])_a$ % absolute	$[\frac{\mu}{\rho}]_{pe}$ (cm ² /g)	$[\frac{\mu}{\rho}]_{R+C}$ (cm ² /g)	f'' (e/atom)
15.2255(12)	78.397(41)	0.029	0.053	77.335(97)	1.062(71)	1.83(12)
14.6257(11)	87.284(57)	0.049	0.066	86.172(84)	1.111(66)	1.95(11)
14.0222(11)	97.767(67)	0.053	0.069	96.601(67)	1.165(56)	2.10(10)
13.4208(10)	109.924(62)	0.035	0.056	108.6997(41)	1.224(49)	2.267(92)
12.8180(11)	124.249(64)	0.026	0.051	122.9607(90)	1.288(45)	2.449(86)
12.4176(11)	135.243(85)	0.045	0.063	133.9091(33)	1.334(43)	2.584(84)
12.0148(12)	147.907(71)	0.019	0.048	146.5242(73)	1.383(43)	2.736(86)
11.6143(13)	161.699(77)	0.017	0.047	160.2643(92)	1.434(45)	2.893(91)
11.2139(14)	177.92(11)	0.050	0.067	176.4381(81)	1.489(48)	3.07(10)
10.8124(15)	195.946(87)	0.006	0.044	194.3975(63)	1.548(53)	3.26(11)
10.4116(16)	218.12(30)	0.130	0.138	216.5165(83)	1.611(60)	3.50(13)
10.0108(18)	247.32(34)	0.133	0.141	245.6427(16)	1.678(70)	3.82(15)
9.6098(19)	34.826(30)	0.075	0.087	33.075(26)	1.750(64)	0.494(18)
9.2089(20)	38.848(31)	0.068	0.081	37.020(48)	1.827(57)	0.529(16)
8.8081(21)	44.102(87)	0.192	0.197	42.192(02)	1.910(52)	0.577(16)
8.4069(23)	50.290(31)	0.042	0.061	48.290(90)	1.999(51)	0.631(16)
8.0065(24)	57.711(72)	0.117	0.126	55.615(11)	2.095(53)	0.692(17)
7.6056(26)	66.672(43)	0.047	0.064	64.473(72)	2.199(41)	0.762(14)
7.2048(27)	77.376(91)	0.110	0.118	75.059(76)	2.317(36)	0.840(13)

of scattering [54] and the presence of harmonic components in the beam [55], respectively.

The four zinc foils were mounted on the specimen stage and could be translated horizontally and vertically as well as rotated about horizontal and vertical axes. The translation movements were reproducible to within 1 μm and ensured that the x-ray beam always passed through the same point of the foil at which the measurements of the mass attenuation coefficients were made. This ensured that the attenuation measurements were always carried out for the same local thickness of the foils.

The micropositioning facility of the stage was also used to raster scan across one of the foils in order to map at a given

energy the attenuation at points regularly distributed over the entire foil. This full-foil mapping made it possible to determine the average mass attenuation coefficient of the foil. Combined with the measured mass and area of the foil, this enabled us to determine the integrated column density of that foil at the point at which the measurements of the mass attenuation at all the various energies were carried out [49].

Four zinc foils of nominal thickness 10, 25, 50, and 100 μm were chosen to provide a range of log attenuation values between 0.5 and 6 across the experimental energy range (Fig. 4). A modified Nordfors criterion [32,56] specifies this as the range of attenuations which leads to an optimal measurement of the mass attenuation coefficients.

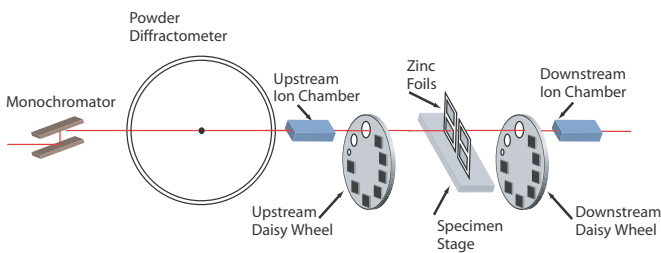


FIG. 2. (Color online) A schematic of the experimental setup. Ion chambers are located upstream and downstream of the specimen stage. Between the specimen stage and the ion chambers, daisy wheels are rotated to insert further absorption foils and apertures into the beam to test for possible systematic corrections. Four zinc foils were mounted on the specimen stage.

III. MEASUREMENT AND ANALYSIS

Analysis of the experimental data can be broken into four independent tasks: determination of the energy, of the mass attenuation coefficient, of sources of systematic error, and of the integrated column density. First the energy of the beam was determined. This was performed by recording powder diffraction patterns of the powder calibration standard Si 640c [57] at regular energy intervals. A calibration curve for the monochromator motor encoder reading against the energy of the beam was determined from the silicon powder diffraction patterns using the method described in [53] and [51].

The second task was the determination of the mass attenuation coefficients on an absolute scale. This involved ion chamber measurements, their normalization, and correction

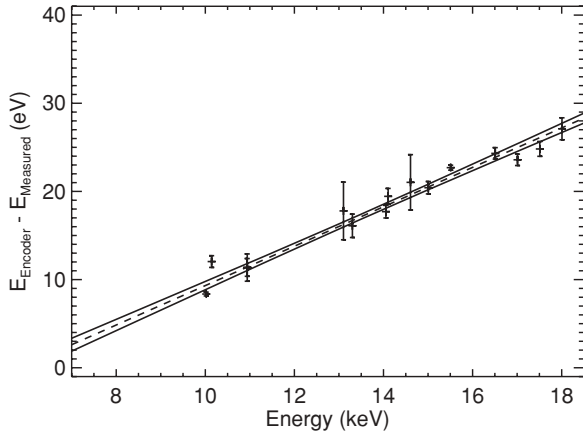


FIG. 3. The difference between the nominal energy of the monochromator encoder reading and the energy determined from the silicon standard powder diffraction patterns at various energies. The correction to the nominal values is consistent with a linear interpolation.

for systematic errors affecting these measurements. The following sections provide details of these procedures. In this experiment we found an important source of systematic error to be the contribution of fluorescent radiation in the energy region immediately above the absorption edge. Another potential source of systematic error—higher order energy harmonic contributions to the monochromatized beam—was minimized by monochromator detuning and corrected for.

A. Energy determination

The energy of the beam was tuned by the Si(111) double-reflection monochromator from 17 to 10 keV monotonically to avoid backlash errors introduced by changing the direction of movement of the monochromator. The motor controlling the angle of the monochromator had an encoder which recorded the angle of the silicon crystal relative to the beam.

In order to determine the energy more accurately, powder diffraction patterns of SRM Si 640c [57] were collected at a number of energies between 10 and 17 keV. By using these energies and the corresponding encoder readings, a calibration was established which proved to be linear (Fig. 3). The differences between the encoder readings and the energies determined from the silicon powder patterns ranged between 26 eV at 18 keV and 8 eV at 10 keV. The energies below 10 keV were determined by extrapolating the energy calibration curve shown in Fig. 3.

B. Measurements of the attenuation

Ion chambers monitored the x-ray beam upstream and downstream of the absorbing foils. The ion chambers were flowed with N_2 gas to reduce the possibility of ion chamber nonlinearity due to ion gas recombination. Between the two ion chambers the beam was attenuated by the foil and also by the air path regions, the ion chamber windows, and the ion chamber gas from the upstream x-ray intensity I_0 to the downstream x-ray flux I . The beam is attenuated by the foil by $\exp(-[\frac{\mu}{\rho}][\rho t]_s)$ where $[\rho t]_s$ is the integrated column density

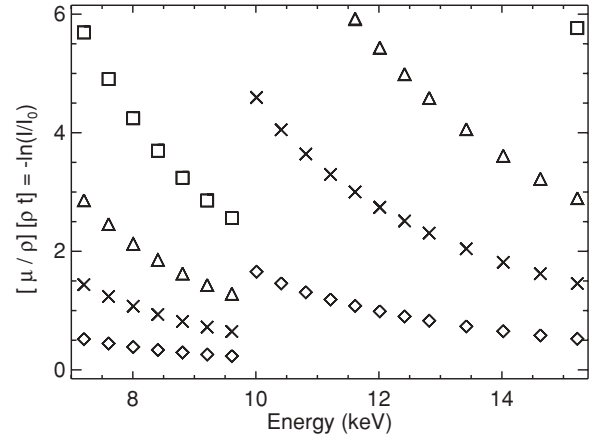


FIG. 4. Measured $[\frac{\mu}{\rho}][\rho t]$ values for the four zinc foils with nominal thicknesses of 10 μm (\diamond), 25 μm (\times), 50 μm (\triangle), and 100 μm (\square). Between 10 and 12 keV, the attenuation of the 50- μm foil was too great to yield accurate results. The attenuation of the 100- μm foil was too great to yield accurate results between 10 and 15 keV.

of the foil and $[\frac{\mu}{\rho}]$ its mass attenuation coefficient. The four different specimen thicknesses are denoted by s . To correct the measured ion chamber intensities for the nonspecimen absorption, upstream and downstream intensities are recorded with the attenuation of the “blank” with the specimen removed. The specimen attenuation is then determined by

$$\exp\left(-\left[\frac{\mu}{\rho}\right][\rho t]_s\right) = \frac{I}{I_0} / \frac{I^B}{I_0^B} \quad s = 1, 2, 3, 4, \quad (1)$$

where I^B are the I_0^B are the ion chamber readings in the absence of the foil [58,59]. All measured intensities were corrected for the “dark current” D (i.e., the current measured when no beam is present). The dark current was measured and subtracted from all ion chamber measurements, so that the specimen attenuation is the exponential of the negative of the log ratio $\ln(R)$:

$$e^{-\ln(R)} = e^{-\left[\frac{\mu}{\rho}\right][\rho t]_s} = \left(\frac{I - D}{I_0 - D_0}\right) / \left(\frac{I^B - D^B}{I_0^B - D_0^B}\right) = \frac{1}{R}. \quad (2)$$

It is essential that the dark current be measured and corrected for in any x-ray absorption experiment, including XAFS and XANES experiments [29,60].

C. Sources of systematic error

1. Fluorescent radiation and scattering

The measured attenuation, $[\frac{\mu}{\rho}]_{\text{local}}$, is affected by the loss of x rays due to scattering and fluorescence of the incident beam by the absorbing foil. In practice, the finite size of the apertures between the upstream and downstream ion chambers results in some angular scattering and fluorescent radiation being included in the intensities. Raleigh and Compton scattering and fluorescent radiation can all contribute to the ion chamber count rate. The scattering and fluorescent radiation signal is a strong function of foil thickness.

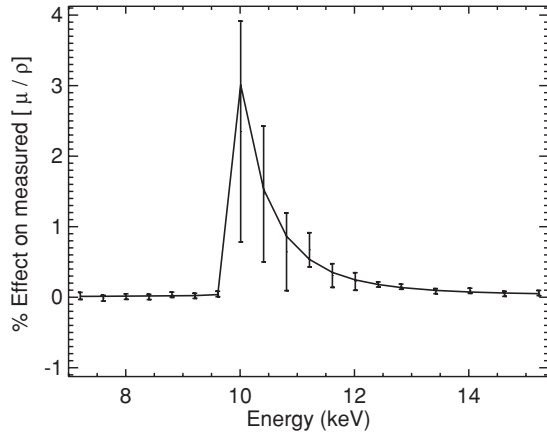


FIG. 5. Percent difference between measurements with two different size apertures due to fluorescent radiation for the 50- μm foil. The difference is highest at the absorption edge and zero within error below the edge and starting about 2 keV above it. The χ_{red}^2 value of the fit is 2.4.

Multiple apertures were mounted on the upstream and downstream daisy wheels in order to determine the aperture size dependence of the ion chamber readings. The largest contribution to aperture-dependent scattering and fluorescent radiation is fluorescence in the absorbing foil. A straightforward *ab initio* model [54] based on the differential absorption of the fluorescence of incident-beam x rays as a function of the aperture size was fitted to the difference between the two aperture measurements in Fig. 5. The model fits the data well as indicated by the χ_r^2 values of the fits.

2. Harmonic contributions and subtraction of dark current

The silicon(111) monochromator Bragg angle was adjusted to select a particular energy from the energy spectrum of the synchrotron. Simultaneously, this angle satisfies the Bragg equation for the higher orders of this reflection with multiples of the fundamental energy. Because the (222) reflection is forbidden, and orders higher than the (333) correspond to negligible or zero contributions, it is the harmonic contribution of the (333) reflection that is of most concern.

Higher energies of the beam have a different mass attenuation coefficient. The contribution from harmonic contamination depends upon the difference between $[\frac{\mu}{\rho}]_f[\rho t]$ of the fundamental energy and its value $[\frac{\mu}{\rho}]_h[\rho t]$ for the harmonic component. Since the difference is thickness-dependent, comparing the measurements for different foil thicknesses with the same $[\frac{\mu}{\rho}]$ is used to determine the higher order contribution to the measured $[\frac{\mu}{\rho}][\rho t]$ and correct for it [55,61,62]. The variation of the recorded log intensity ratio with foil thickness due to the third-order harmonic component is given by the second term of

$$\exp\left(\left[\frac{\mu}{\rho}\right][\rho t]\right) = (1-x)\exp\left(\left[\frac{\mu}{\rho}\right]_f[\rho t]\right) + x\exp\left(\left[\frac{\mu}{\rho}\right]_h[\rho t]\right), \quad (3)$$

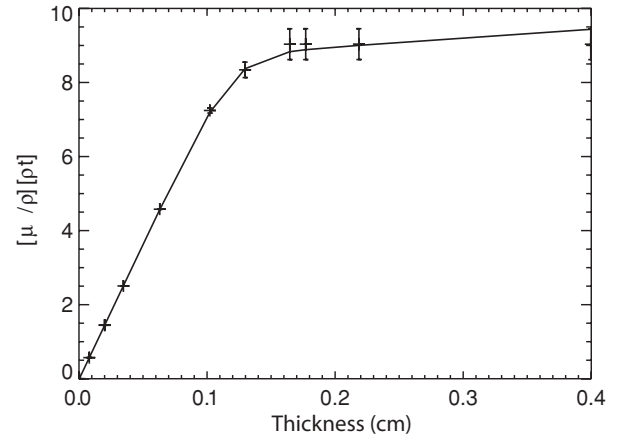


FIG. 6. The model of the harmonic contribution to the attenuation $[\frac{\mu}{\rho}][\rho t]$ of the multiple aluminium foils mounted on the daisy wheel at 9.61 keV. The model of Eq. (3) fitted the experimental data with a small harmonic fraction of $x = 0.0310\% \pm 0.0064\%$.

where x is the fraction of the harmonic component in the beam. For very thick foils, both the fundamental and harmonic components of the beam become attenuated so that no counts are detected by the downstream ion chamber [63]. A term ΔD is included to account for this nonlinearity:

$$\exp\left(\left[\frac{\mu}{\rho}\right][\rho t]\right) = \frac{I - D - \Delta D}{I_0 - D_0}, \quad (4)$$

where ΔD is the error in the downstream ion chamber dark current.

Aluminium foils were mounted on daisy wheels to test for the presence of harmonic components in the beam. Figure 6 shows the fitted function of Eq. (3) at 9.61 keV. At this energy, the model is well described with a higher order harmonic component accounting for $0.0310\% \pm 0.0064\%$ of the beam. The slopes of the two linear sections of the figure correspond essentially to the values of $[\frac{\mu}{\rho}]$ for the fundamental and harmonic x rays, respectively; this fact can be used as a test of the final curve after correction for dark current. At other measured energies the harmonic component was found to be less than 0.031%, except for the lowest energy (7.2 keV) where the harmonic component was greatest with $0.31\% \pm 0.06\%$. Corrections were made to the measured $[\frac{\mu}{\rho}][\rho t]$ values to account for the harmonic component according to Eq. (3).

3. Bandwidth

The monochromated x-ray beam has a small energy bandwidth. Previous measurements [64] have found that the energy bandwidth is an important source of error in absorption experiments when the gradient of the mass attenuation coefficient is significant, particularly at the absorption edge. The results presented here are on a coarser energy grid and all measurements—except possibly those between 10.0 and 10.2 keV—are made in regions where the mass attenuation coefficient is varying slowly. Accordingly, we have not observed any bandwidth effect. If present, the bandwidth effect would likely only affect the measurement made at 10.0108 keV. An experiment on a much finer energy grid is

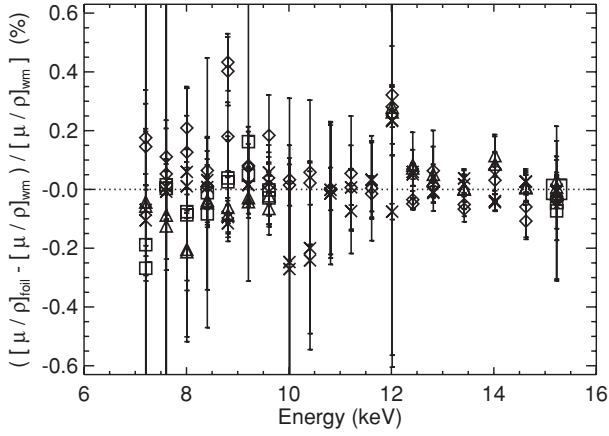


FIG. 7. Differences between $[\frac{\mu}{\rho}]$ of the foils and their weighted mean at each energy after determination of foil-integrated column densities. By assuming a density of zinc metal foil of $7.13 \pm 0.01 \text{ g cm}^{-3}$ [66], the local thicknesses of the four foils at the points where the x-ray beam passed through the foils were determined to be $102.91 \pm 0.09 \mu\text{m}$ (\square), $51.69 \pm 0.03 \mu\text{m}$ (\triangle), $26.01 \pm 0.015 \mu\text{m}$ (\times), and $9.347 \pm 0.006 \mu\text{m}$ (\diamond), rather than the nominal thicknesses of 100, 50, 25, and $10 \mu\text{m}$. The average thickness of the nominally 50- μm -thick foil was $51.597 \pm 0.014 \mu\text{m}$ (\triangle). The χ^2 value of the fit was 1.23. The foil mapping measurement is indicated by the large square at 15.2 keV.

recommended and would probably require such a correction in the immediate vicinity of the edge.

4. Roughness

Roughness of the foil specimens is a potential source of error in absorption experiments [30]. The effect of roughness is dependent on the thickness of the foil, as the percentage magnitude of the correction is inversely proportional to thickness [65]. The thinnest foil used in these measurement was $9.36 \mu\text{m}$ thick. Previous experiments have seen the roughness effect for foils thinner than $5 \mu\text{m}$.

The signature expected in Fig. 7 due to a systematic effect of roughness would be a large deviation in the weighted mean at the edge, which would steadily decrease with increasing energy above the absorption edge. We have observed such a signature in earlier studies. However, Fig. 7 does not contain any thickness-dependent residual patterns to suggest a systematic residual due to roughness. There is some deviation of the thinnest foil below the edge, but this signature is not consistent with a roughness correction because the deviation is not present above the absorption edge.

D. Integrated column density

The integrated column density $[\rho t]_{xy}$ is the density at point (x, y) of the foil integrated along the path of the x-ray beam and averaged over the x-ray beam cross section,

$$[\rho t]_{xy} = \int_0^t [\rho]_{xyz} dz, \quad (5)$$

where $[\rho]_{xyz}$ is the density of the foil at any given point. The beam travels in the z direction and passes through the foil at the point (x, y) . Hence this is similar to a profilometer or

micrometer definition of thickness but relates to the actual measurement and possible variations in density, roughness, or void structures in the material under investigation. Given the local absolute value of the integrated column density of the mapped foil, the integrated column densities of the other experimental foils were derived from a comparison of their measured attenuations with that of the mapped foil by minimizing χ^2 deviations of the weighted mean of the measured $[\frac{\mu}{\rho}][\rho t]$ values at each energy [49]:

$$\chi^2 = \sum_E \sum_F \left(\frac{\left[\frac{\mu}{\rho} \right]_{E_i F_j} - \left[\frac{\mu}{\rho} \right]_{E_i}}{\sigma \left(\left[\frac{\mu}{\rho} \right]_{E_i F_j} \right)} \right)^2. \quad (6)$$

Equation (6) determines the χ^2 value of the weighted mean of the attenuation coefficients of the foils at each experimental energy E_i as a function of the foil F_j . Figure 7 shows the residuals from the fitting procedure. This procedure was carried out only after all of the thickness-dependent systematic errors considered in the earlier sections had been corrected for.

E. Full-foil mapping of the attenuation

The largest source of uncertainty in measurements of mass attenuation coefficients using metal foils is often in the absolute determination of the local integrated column density [30,67], defined as the integral of the density along the path traversed by the x-ray beam [49]. To determine the average integrated column density of the foil, $[\rho t]_{av}$, one measures the total mass and area of the foil:

$$[\rho t]_{av} = \frac{m}{A}. \quad (7)$$

The foils were weighed on a microgram Mettler microbalance to determine their mass m with an error of $\Delta m/m$ of 0.002%. The perimeter of the foils was mapped at 172 points using an optical comparator to determine their area A with an error $\Delta A/A$ of 0.026%. The local integrated column density is determined from $[\rho t]_{av}$ by

$$[\rho t]_{local} = \frac{\left[\frac{\mu}{\rho} \right] [\rho t]_{local}}{\left[\frac{\mu}{\rho} \right] [\rho t]_{av}} [\rho t]_{av} = \frac{[\ln(R)]_{local} m}{[\ln(R)]_{av} A}. \quad (8)$$

To determine the local integrated column density, we modify the prescription given in [49] as follows. The 50- μm -thick foil was mapped by translating the foil vertically and horizontally about the x-ray beam at 15.2 keV. Figure 8 shows the local value of $[\ln(R)]_{local}$, which is proportional to the map of the relative local integrated column density $[\rho t]_{local}$. The foil is mapped by the x-ray beam in 2-mm horizontal steps and 0.5-mm vertical steps. At each step the measurements were repeated ten times to determine $[\ln(R)]_{local}$ with an uncertainty σ given by the standard error of the measurements. For the central point 100 repeated measurements yielded a standard error $\sigma_{[\ln(R)]_{local}} = 0.0058\%$.

The foil-only area was maximized by supporting the foil with a newly designed Perspex holder that held the foil along two edges only [63]. This avoided the need to fit a foil holder to the attenuation profile. The average over the foil-only region

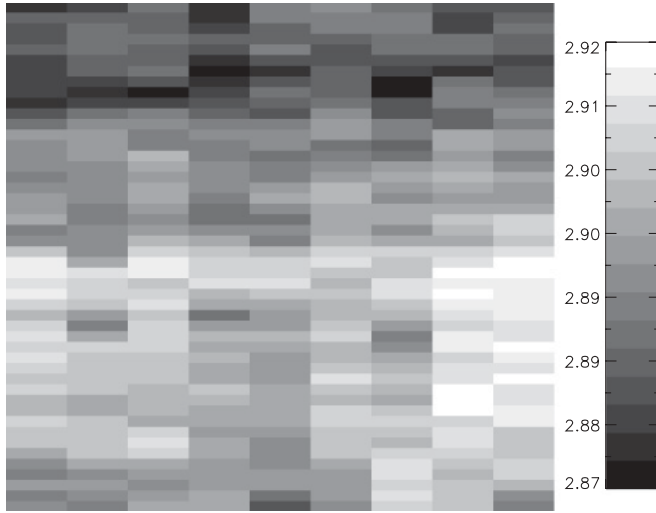


FIG. 8. The relative local attenuation of the foil mapped by the x-ray beam. The rolling seen in the integrated column density is representative of the structure of the foil.

yields an uncertainty in $[\ln(R)]_{\text{av}}$ as the standard deviation of $[\rho t]_{\text{av}}$:

$$\sigma_{[\ln(R)]_{\text{av}}} = \frac{\sqrt{\sum \sigma^2}}{\sqrt{N}}, \quad (9)$$

where N is the number of points mapped across the foil. The standard deviation of $[\ln(R)]_{\text{av}}$ following Eq. (9) was 0.024%.

At the edges of the foil, only a fraction of the beam, f , passes through the foil while the remaining fraction, $(1 - f)$, passed through either the Perspex holder or air. For each of the four foil edges, a model estimated the fraction of the beam passing through the foil at each point along the edge under the assumption that the edges were straight lines. In the central region of the foil, the beam passed through only foil and therefore f is equal to one. The error in the value of $[\ln(R)]_{\text{av}}$ due to the uncertainty of each point mapped is calculated as the area-weighted standard deviation of the points:

$$\sigma_{[\ln(R)]_{\text{av}}} = \frac{\sqrt{\sum \sigma^2 f}}{\sqrt{\sum f}}. \quad (10)$$

The standard deviation of $[\ln(R)]_{\text{av}}$ following Eq. (10) was 0.035%. The uncertainty associated with the integrated column density determination $\sigma_{[\rho t]_{\text{local}}}$ is then

$$\left[\frac{\sigma_{[\rho t]_{\text{local}}}}{[\rho t]_{\text{local}}} \right]^2 = \left[\frac{\sigma_{[\ln(R)]_{\text{local}}}}{[\ln(R)]_{\text{local}}} \right]^2 + \left[\frac{\Delta A}{A} \right]^2 + \left[\frac{\Delta m}{m} \right]^2 + \left[\frac{\sigma_{[\ln(R)]_{\text{av}}}}{[\ln(R)]_{\text{av}}} \right]^2. \quad (11)$$

Including the edge points, which generally had larger uncertainties than the central points, the final percentage uncertainty of the local integrated column density was found to be 0.044%. The two terms which contributed the most to the final uncertainty were the area-weighted standard deviation, which accounted for 0.035%, and the uncertainty in the area of the foil, which accounted for 0.026%.

IV. TABULATION OF RESULTS

Table I presents the measured mass attenuation coefficients as a function of the photon energy with the total uncertainty in least significant figures in parentheses. The percent relative accuracy $\sigma([\frac{\mu}{\rho}])_r$ is the weighted standard deviation, as just discussed, relevant when comparing the mass attenuation coefficients presented here with measurements made on a relative energy scale, such as in XAFS or XANES measurements. The percent absolute accuracy $\sigma([\frac{\mu}{\rho}])_a$ is the percentage uncertainty in the weighted standard deviation including the uncertainty in the determination of the absolute integrated column density. The percent absolute accuracy is the error which is relevant in a comparison of our measured mass attenuation coefficients with theory or other experimental measurements.

The imaginary components of the atomic form factors are related to the photoelectric mass absorption coefficients by

$$f'' = \frac{EuA \left[\frac{\mu}{\rho} \right]_{\text{pe}}}{2hcR_e}, \quad (12)$$

where E is the energy, u the atomic mass unit, A the atomic mass, and R_e the classical electron radius, and the other symbols have their usual meanings. The imaginary part of the form factor f'' is calculated from the photoionization cross section after subtracting the Rayleigh and Compton scattering contributions, $[\frac{\mu}{\rho}]_{\text{R+C}}$, obtained from the FFAST calculation [13–15]. The uncertainty in $[\frac{\mu}{\rho}]_{\text{R+C}}$ is estimated to be half the discrepancy between the values tabulated in XCOM and FFAST and is included in the calculation of the uncertainty of f'' .

V. COMPARISON WITH THEORY

NIST recommends two theoretical tabulations for the photoelectric, Compton, and Rayleigh scattering of x rays, which are used to calculate mass attenuation coefficients. Other scattering contributions are negligible in this energy range. These are plotted in Fig. 9 with our measurements.

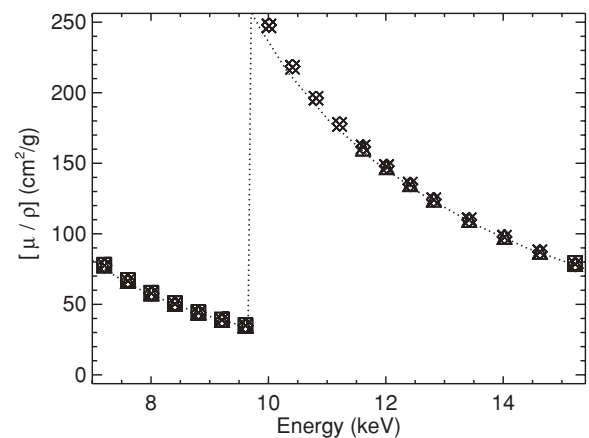


FIG. 9. The mass attenuation coefficients given by FFAST (dotted line) and our measurements in cm^2/g . On the scale of this figure the results of the measurements with the four foils coincide. Uncertainties are smaller than the symbols marking the measured values.

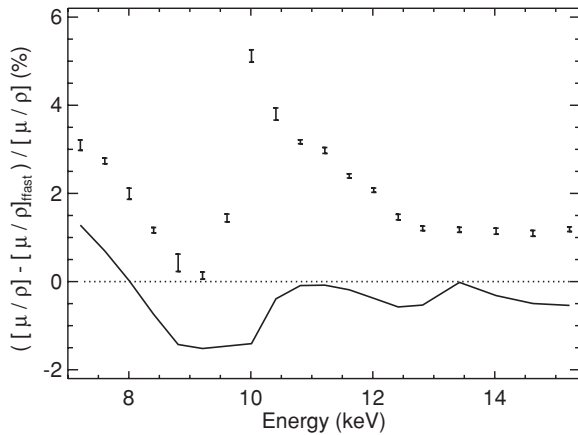


FIG. 10. Percent deviation of the experimental mass attenuation coefficients from FFAST [15]. The solid line shows XCOM [11,12] values relative to FFAST. There is a significant unexplained discrepancy with all theories, especially over the region approximately 2 keV above the absorption edge (9.623 keV). In general the earlier experimental data were unreliable at the level claimed, so agreement with theory has in fact improved with these experimental results. Uncertainties are smaller than the symbols marking the measured values. Note that there is evidence that FFAST is moderately consistent across the energy range, but with significant excursions, while XCOM appears offset across this energy range but perhaps with fewer excursions.

Figure 10 shows a general comparison of mass attenuation coefficients calculated by FFAST [14] with our measurements. Above 12.75 keV the experimental results agree with FFAST and XCOM within the 1% quoted uncertainty of the tabulations at these energies. In the edge region there is significant deviation between theory and experiment. Below 12.75 keV the discrepancies between FFAST and our measurements increase, reaching a maximum just before the absorption edge. Below the absorption edge the discrepancy decreases to zero and then starts to rise again. Its rising trend as a percentage is parallel to the rise of the XCOM values.

The FFAST calculations [14] are Dirac-Hartree-Fock relativistic self-consistent field computations using the Kohn-Sham potential for effective screening, whereas XCOM [16] uses Hartree-Slater nonrelativistic wave functions with relativistic corrections included in perturbation following Scofield, including via alternative databases a correction for the relativistic amplitude at the origin. Creagh uses relativistic wave functions including multipole transition contributions as discussed in [20]; while Henke uses a semi-empirical evaluated database from theoretical and experimental sources [21], with dominant theory following Scofield but with deviations perhaps dominated by evaluation of earlier experimental contributions. The last two tabulations are presented in Fig. 1, while Fig. 10 provides the improved comparison.

Relativistic corrections have been discussed in detail in the theoretical databases, with perhaps the dominant effects discussed in the literature being on the offset of the real component of the form factor [68] and the contribution of multipolar amplitudes at medium atomic number [69]. These particular effects are not responsible for the discrepancy seen in Fig. 10. The level of convergence of the calculation, however,

can lead to discrepancies with an oscillatory structure [14]. This effect is largest near absorption edges. Both calculations make use of the independent particle approximation.

QED does play a role, especially to first order in the energy levels and ionization edges of the quantum systems. However, any such contribution to deviations is dominated by solid-state effects including near-edge shifts of the wave functions due to bonding and band structure. The Kohn-Sham method in general has approximations relating to ionization energies which dominate over QED shifts, and which we are addressing in other work. Hence the discrepancies are not, at this level, due to QED effects.

There is a peculiar trend of this in relation to the edge [30–34,44]. So far only molybdenum, silver, copper, and tin have been carefully investigated in this manner, and there are key differences among the patterns observed for each. In the near-edge region none of the theoretical approaches produces values which agree with the measured mass attenuation coefficient and there is a strong need for a review of the calculations. One of the particular problems is that numerous assumptions of different types might explain part of the discrepancies. The improved accuracy of our measurements provides strong motivation for further review of theory, particularly in the K-edge region, a region which is important for many x-ray techniques including XAFS and XANES.

Limitations of convergence of the theoretical wavefunctions and eigenvalues for energy near absorption edges can lead to oscillations in the calculated spectrum [14]. However, the oscillatory structure seen in Fig. 10 is quite plausibly due to many-body effects. In the near-edge region many-body effects such as inelastic losses, local-field effects [70] and core-hole amplitudes, and thermal vibrations can contribute significantly to the total scattering cross section, extrinsic losses in the propagation of the photoelectron, and intrinsic losses such as shake-up and shake-off [71].

There has been recent renewed interest in theoretical models for calculating XAS and optical constants in the United States, France, and Australia in particular [72]. An improved model for calculating XAS, FEFF9, addresses many-body effects more accurately than previous models [73]. Unlike previous versions of FEFF, FEFF9 is an *ab initio* model which can calculate the total scattering cross section, and these high-accuracy data sets have been used as test cases to develop and understand theoretical limitations over the past five years. In this model the dielectric and vibrational response of the system is used to account for many-body effects from first principles [73]. Earlier solid-state and atomic theoretical approaches relied on simplified models for many-body effects. In recent work, one of the most advanced theoretical solid-state groups has investigated the effects of (i) core-hole lifetimes; (ii) threshold energy cutoff; (iii) the so-called edge singularity effect; (iv) multipole effects; and (v) embedded atomic background and solid-state local interactions [74]. These studies are beginning to unearth contributions to the observed discrepancies, but much more work is required.

Another *ab initio* model for XAS, the finite difference model for near edge structure (FDMNES) [9], can also be compared to other high-accuracy measurements. Such a comparison led to a suggested improvement in the implementation of thermal broadening [75].

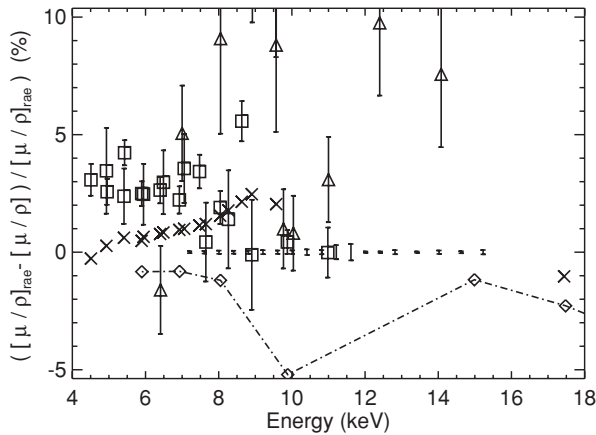


FIG. 11. Percent deviation of earlier experimental and theoretical results for the mass attenuation coefficients of zinc relative to the current experimental results. Symbols are as in Fig. 1. Shown are Creagh and McAuley [20] values with \times marking energies tabulated in the International Tables for Crystallography, and the dot-dash line shows the experimental-theoretical values of Henke *et al.* [21] with the \diamond symbol marking the tabulated energies.

Figure 11 compares other experimental results to our results. A significant offset is seen to the data tabulated by Creagh and McAuley [20], while a larger excursion in the opposite direction is seen for the Henke tabulation. While some experimental data do overlap the current results, most are inconsistent with their own adjacent points and show errors of up to 9%. Even below the edge there is a significant offset of about 2.5% between our measurements and the measurements of Unonius and Suortti [19]. Despite the larger uncertainties reported previously, the spread of those results is sometimes

larger than the error bars. The spread and reported uncertainty of previous studies of zinc means that no distinction between the different theoretical approaches was previously possible. The offset between measurements made by different groups in Fig. 11 is of a similar magnitude to the offset seen between different theoretical calculations. We have addressed this need with higher accuracy measurements. High-accuracy measurement provides a baseline by which the discrepancies in the mass attenuation coefficients can be compared.

VI. CONCLUSION

The mass attenuation coefficients of zinc have been determined on an absolute scale with an accuracy of 0.044%–0.197% and generally to better than 0.12%, with bending-magnet synchrotron x rays. These are the most accurate such measurements performed on a bending-magnet, following from the increased accuracy of the integrated column density determination. Modifications to the foil holder led to a reduction in the error of the measurement. The FFAST and XCOM tabulations agree with measurements at energies above 12.75 keV within the 1% error quoted for the FFAST and XCOM values in this region [13–15]. A significant discrepancy above and below the K-edge is consistent with our previous studies. Further theoretical work is needed to explain this observed discrepancy. A further experimental study with higher energy resolution to investigate the near-edge structure would be desirable.

ACKNOWLEDGMENTS

The authors gratefully acknowledge the support of the ARC and ASRP with grants for this work and the ANBF beamline staff for the experimental beam time.

-
- [1] S. Heredia-Avalos, R. Garcia-Molina, J. M. Fernández-Varea, and I. Abril, *Phys. Rev. A* **72**, 052902 (2005).
- [2] C. C. Montanari, J. E. Miraglia, S. Heredia-Avalos, R. Garcia-Molina, and I. Abril, *Phys. Rev. A* **75**, 022903 (2007).
- [3] V. Kladko, L. Datsenko, V. Machulin, J. Domagala, P. Lytvyn, J. Bak-Misiuk, A. Kuchuk, and A. Korchovyi, *J. Appl. Crystallogr.* **37**, 150 (2004).
- [4] J. H. Beaumont and M. Hart, *J. Phys. E* **7**, 823 (1974).
- [5] K. Ham, H. Jin, R. Al-Raoush, X. Xie, C. S. Willson, G. R. Byerly, L. S. Simeral, M. L. Rivers, R. L. Kurtz, and L. G. Butler, *Chem Mater.* **16**, 4032 (2004).
- [6] W. S. M. Werner, *Phys. Rev. B* **74**, 075421 (2006).
- [7] A. N. Hoppersky, I. D. Petrov, A. M. Nadolinsky, V. A. Yavna, and R. V. Koneev, *J. Phys. B* **37**, 3313 (2004).
- [8] P. H.-L. Sit, C. Bellin, B. Barbiellini, D. Testemale, J. L. Hazemann, T. Buslaps, N. Marzari, and A. Shukla, *Phys. Rev. B* **76**, 245413 (2007).
- [9] Y. Joly, *Phys. Rev. B* **63**, 125120 (2001).
- [10] F. M. Hossain, D. P. Riley, and G. E. Murch, *Phys. Rev. B* **72**, 235101 (2005).
- [11] M. J. Berger and J. H. Hubbell, *XCOM: Photon Cross Sections on a Personal Computer*, NBSIR 87-3597 (National Bureau of Standards, Gaithersburg, MD, 1987).
- [12] J. H. Hubbell, *Int. J. Appl. Radiat. Isotopes* **33**, 1269 (1982).
- [13] C. T. Chantler, *J. Phys. Chem. Ref. Data* **24**, 71 (1995).
- [14] C. T. Chantler, *J. Phys. Chem. Ref. Data* **29**, 597 (2000).
- [15] C. T. Chantler, K. Olsen, R. A. Dragoset, A. R. Kishore, S. A. Kotochigova, and D. S. Zucker, *X-Ray Form Factor, Attenuation and Scattering Tables (version 2.0)* (National Institute of Standards and Technology, Gaithersburg, MD, 2009), <http://physics.nist.gov/ffast>.
- [16] E. B. Saloman, J. H. Hubbell, and J. H. Scofield, *At. Data Nucl. Data Tables* **38**, 1 (1988).
- [17] S. Nayak and N. Badiger, *J. Phys. B* **39**, 2893 (2006).
- [18] J. I. Hopkins, *J. Appl. Phys.* **30**, 185 (1959).
- [19] L. Unonius and P. Suortti, *J. Appl. Cryst.* **22**, 46 (1989).
- [20] D. C. Creagh and W. J. McAuley, in *International Tables for Crystallography*, edited by A. J. C. Wilson (Kluwer Academic, Boston, 1992).
- [21] B. L. Henke, E. M. Gullikson, and J. C. Davis, *At. Data Nucl. Data Tables* **54**, 181 (1993).
- [22] J. J. Rehr, R. C. Albers, and S. I. Zabinsky, *Phys. Rev. Lett.* **69**, 3397 (1992).
- [23] A. Karabulut, A. Gurol, G. Budak, and R. Polat, *Eur. Phys. J. D* **21**, 57 (2002).
- [24] A. S. Bennal and N. M. Badiger, *J. Phys. B* **40**, 2189 (2007).

- [25] N. Kaya, A. Kobya, E. Tıraşoğlu, and G. Apaydin, *J. Phys. B* **41**, 225003 (2008).
- [26] A. Karabulut, A. Gurol, G. Budak, and M. Ertugrul, *Nucl. Instrum. Methods Phys. Res. B* **227**, 485 (2005).
- [27] J. Brugger, B. Etschmann, W. Liu, D. Testemale, J. L. Hazemann, H. Emerich, W. van Beek, and O. Proux, *Geochim. Cosmochim. Acta* **71**, 4920 (2007).
- [28] D. C. Creagh and J. H. Hubbell, *Acta Crystallogr.* **43**, 102 (1987).
- [29] D. C. Creagh and J. H. Hubbell, *Acta Crystallogr.* **46**, 402 (1990).
- [30] M. D. de Jonge, C. Q. Tran, C. T. Chantler, Z. Barnea, B. B. Dhal, D. J. Cookson, W.-K. Lee, and A. Mashayekhi, *Phys. Rev. A* **71**, 032702 (2005).
- [31] C. Q. Tran, C. T. Chantler, Z. Barnea, M. D. de Jonge, B. B. Dhal, C. Chung, D. Paterson, P. Lee, J. Wang, and D. J. Cookson, *J. Phys. B* **38**, 89 (2005).
- [32] C. T. Chantler, C. Q. Tran, Z. Barnea, D. Paterson, D. J. Cookson, and D. X. Balaic, *Phys. Rev. A* **64**, 062506 (2001).
- [33] M. D. de Jonge *et al.*, *Phys. Rev. A* **75**, 032702 (2007).
- [34] J. L. Glover, C. T. Chantler, Z. Barnea, N. A. Rae, C. Q. Tran, D. C. Creagh, D. Paterson, and B. B. Dhal, *Phys. Rev. A* **78**, 052902 (2008).
- [35] A. Mihelič, A. Kodre, I. Arčon, and J. P. Gomilšek, *Acta Chim. Slov.* **51**, 33 (2004).
- [36] K. Hatada and J. Chaboy, *Phys. Rev. B* **76**, 104411 (2007).
- [37] J. Chaboy, N. Nakajima, and Y. Tezuka, *J. Phys.: Condens. Matter* **19**, 266206 (2007).
- [38] M. P. Ruffoni, R. F. Pettifer, S. Pascarelli, and O. Mathon, *J. Synchrotron Radiat.* **14**, 169 (2006).
- [39] E. Casnati, C. Baraldi, and A. Tartari, *Phys. Rev. A* **42**, 2627 (1990).
- [40] L. Gerward, G. Thuesen, S. Jensen, and I. Alstrup, *Acta Crystallogr. A* **35**, 852 (1979).
- [41] L. Gerward, *J. Phys. B* **22**, 1963 (1989).
- [42] A. Kodre, J. Padežnik Gomilšek, A. Mihelič, and I. Arčon, *Rad. Phys. Chem.* **75**, 188 (2006).
- [43] C. T. Chantler, *Eur. Phys. J. Spec. Top.* **169**, 147 (2009).
- [44] C. T. Chantler and Z. Barnea, *J. Phys.: Condens. Matter* **11**, 4087 (1999).
- [45] C. Q. Tran, C. T. Chantler, and Z. Barnea, *Phys. Rev. Lett.* **90**, 257401 (2003).
- [46] C. Q. Tran, C. T. Chantler, Z. Barnea, D. Paterson, and D. J. Cookson, *Phys. Rev. A* **67**, 042716 (2003).
- [47] C. T. Chantler, C. Q. Tran, D. Paterson, D. J. Cookson, and Z. Barnea, *Phys. Lett.* **A286**, 338 (2001).
- [48] J. F. Mika, L. J. Martin, and Z. Barnea, *J. Phys. C* **18**, 5215 (1985).
- [49] M. D. de Jonge, Z. Barnea, C. T. Chantler, and C. Q. Tran, *Meas. Sci. Technol.* **15**, 1811 (2004).
- [50] L. F. Smale, C. T. Chantler, M. D. de Jonge, Z. Barnea, and C. Q. Tran, *Rad. Phys. Chem.* **75**, 1559 (2006).
- [51] C. T. Chantler, N. A. Rae, and C. Q. Tran, *J. Appl. Crystallogr.* **40**, 232 (2007).
- [52] Z. Barnea, D. C. Creagh, T. J. Davis, R. F. Garrett, S. Janky, A. W. Stevenson, and S. W. Wilkins, *Rev. Sci. Instrum.* **63**, 1069 (1992).
- [53] N. A. Rae, C. T. Chantler, C. Q. Tran, and Z. Barnea, *Rad. Phys. Chem.* **75**, 2063 (2006).
- [54] C. Q. Tran, M. D. de Jonge, Z. Barnea, and C. T. Chantler, *J. Phys. B* **37**, 3163 (2004).
- [55] C. Q. Tran, Z. Barnea, M. D. de Jonge, B. B. Dhal, D. Paterson, D. J. Cookson, and C. T. Chantler, *X-Ray Spectrom.* **32**, 69 (2003).
- [56] B. Nordfors, *Ark. Fys.* **18**, 37 (1960).
- [57] J. P. Cline, R. D. Deslattes, J. L. Staudenmann, E. G. Kessler, L. T. Hudson, A. Henins, and R. W. Cheary (NIST, Gaithersburg, MD, 2000).
- [58] C. T. Chantler, C. Q. Tran, D. Paterson, Z. Barnea, and D. J. Cookson, *X-Ray Spectrom.* **29**, 449 (2000).
- [59] C. T. Chantler, C. Q. Tran, D. Paterson, D. J. Cookson, and Z. Barnea, *X-Ray Spectrom.* **29**, 459 (2000).
- [60] J. L. Glover and C. T. Chantler, *Meas. Sci. Technol.* **18**, 2916 (2007).
- [61] M. D. de Jonge, C. Q. Tran, C. T. Chantler, and Z. Barnea, *Opt. Eng.* **45**, 046501 (2006).
- [62] Z. Barnea and J. Mohyla, *J. Appl. Crystallogr.* **7**, 298 (1974).
- [63] M. D. de Jonge, Ph.D. thesis, University of Melbourne, Parkville, Australia, 2005.
- [64] M. D. de Jonge, Z. Barnea, C. Q. Tran, and C. T. Chantler, *Phys. Rev. A* **69**, 022717 (2004).
- [65] J. L. Glover, C. T. Chantler, and M. D. de Jonge, *Phys. Lett.* **A373**, 1177 (2009).
- [66] D. R. Lide, *CRC Handbook of Chemistry and Physics* (CRC, Boca Raton, 1993).
- [67] C. Q. Tran, Z. Barnea, C. T. Chantler, and M. D. de Jonge, *Rev. Sci. Instrum.* **75**, 2943 (2004).
- [68] D. C. Creagh, *Nucl. Instrum. Methods A* **295**, 417 (1990).
- [69] P. P. Kane, L. Kissel, R. H. Pratt, and S. C. Roy, *Phys. Rep.* **140**, 75 (1986).
- [70] J. J. Rehr, *Rad. Phys. Chem.* **75**, 1547 (2006).
- [71] L. Campbell, L. Hedin, J. J. Rehr, and W. Bardyszewski, *Phys. Rev. B* **65**, 064107 (2002).
- [72] J. J. Rehr, M. P. Prange, and J. J. Kas, *J. Phys. Conf. Ser.* **190**, 012001 (2009).
- [73] J. J. Rehr, J. J. Kas, M. P. Prange, A. P. Sorini, Y. Takimoto, and F. Vila, *C. R. Phys.* **10**, 548 (2009).
- [74] J. J. Kas, J. J. Rehr, J. L. Glover, and C. T. Chantler, *Nucl. Instrum. Methods A* (2010, in press).
- [75] J. D. Bourke, C. T. Chantler, and C. Witte, *Phys. Lett.* **A360**, 702 (2007).